remote sensing

MDPI

Article

Leveraging the Potential of PRISMA Hyperspectral Data for Forest Tree Species Classification: A Case Study in Southern Italy

Gabriele Delogu [1,2], Miriam Perretta [3,4], Eros Caputi [1,2], Alessio Patriarca [2], Cassandra Carroll Funsten [3], Fabio Recanatesi [2], Maria Nicolina Ripa [2] and Lorenzo Boccia [3,4,*]

1 Department of Economics, Engineering, Society and Business Organization (DEIM), Tuscia University, Via del Paradiso, 47, 01100 Viterbo, Italy; gabriele.delogu@unitus.it (G.D.); eros.caputi@unitus.it (E.C.)
2 Department of Agricultural and Forestry Sciences (DAFNE), Tuscia University, Via S. Camillo de Lellis, 01100 Viterbo, Italy; alessio.patriarca@unitus.it (A.P.); fabio.rec@unitus.it (F.R.); nripa@unitus.it (M.N.R.)
3 Department of Architecture, University of Naples Federico II, Via Forno Vecchio, 36, 80134 Naples, Italy; miriam.perretta@unina.it (M.P.); cassandracarroll.funsten@unina.it (C.C.F.)
4 National Biodiversity Future Center (NBFC), 90133 Palermo, Italy
* Correspondence: lorenzo.boccia@unina.it; Tel.: +39-0812-539-151

Abstract: Hyperspectral imagery and advanced classification techniques can significantly enhance remote sensing's role in forest monitoring. Thanks to recent missions, such as the Italian Space Agency's PRISMA (PRecursore IperSpettrale della Missione Applicativa—Hyperspectral PRecursor of the Application Mission), hyperspectral data in narrow bands spanning visible/near infrared to shortwave infrared are now available. In this study, hyperspectral data from PRISMA were used with the aim of testing the applicability of PRISMA with different band sizes to classify tree species in highly biodiverse forest environments. The Serre Regional Park in southern Italy was used as a case study. The classification focused on forest category classes based on the predominant tree species in sample plots. Ground truth data were collected using a global positioning system together with a smartphone application to test its contribution to facilitating field data collection. The final result, measured on a test dataset, showed an F1 greater than 0.75 for four classes: fir (0.81), pine (0.77), beech (0.90), and holm oak (0.82). Beech forests showed the highest accuracy (0.92), while chestnut forests (0.68) and a mixed class of hygrophilous species (0.69) showed lower accuracy. These results demonstrate the potential of hyperspectral spaceborne data for identifying trends in spectral signatures for forest tree classification.

Keywords: PRISMA sensor; hyperspectral data; forest cover classification; forestry monitoring; tree stands; tree species

Citation: Delogu, G.; Perretta, M.; Caputi, E.; Patriarca, A.; Funsten, C.C.; Recanatesi, F.; Ripa, M.N.; Boccia, L. Leveraging the Potential of PRISMA Hyperspectral Data for Forest Tree Species Classification: A Case Study in Southern Italy. *Remote Sens.* **2024**, *16*, 4788. https://doi.org/10.3390/rs16244788

Academic Editors: Micol Rossini, Hongyan Liu, Ying Qu, Boyi Liang and Jiangzhou Xia

Received: 15 November 2024
Revised: 15 December 2024
Accepted: 20 December 2024
Published: 22 December 2024

1. Introduction

Environmental and biodiversity monitoring have become essential to preserving the planet in the face of human activity and climate change [1–3]. Forests are reservoirs of biodiversity [4] and deserve special attention because the benefits humans receive from nature depend on their ecosystem functionality [5,6]. Automated processes can support natural resource conservation, management, and promotion tasks by facilitating the large-scale availability of detailed and up-to-date land use (LU) and land cover (LC) information [7]. In an era of global change, vegetation maps are critical for understanding and managing local to global biodiversity patterns [8]. Remote sensing (RS) is a practical and feasible solution for deforestation and forest degradation monitoring, and policies such as REDD (reducing emissions from deforestation and forest degradation in developing countries) could be based on above-ground biomass mapping alongside conventional field sampling [9].

The potential of hyperspectral data to contribute to innovative research has been the subject of growing attention. Up until now, with the exception of NASA's pioneer Hyperion

mission [10], these studies have been based on airborne data [11], or in some cases, on unmanned aerial vehicle (UAV) data [12]. However, recent hyperspectral satellite missions such as PRISMA [13] and EnMAP [14], launched in 2019 and 2022, respectively, have added new tools to the field of Earth observation (EO). PRISMA hyperspectral imagery (HSI) has 240 bands with a bandwidth of 12 nm or less. The bands range from the visible/near infrared spectrum (400–1010 nm) (VNIR) to the shortwave infrared spectrum (920–2505 nm) (SWIR). The swath width at nadir is 30 km, the ground sampling distance (GSD) is 30 m for the hyperspectral bands and 5 m for the panchromatic band, and the radiometric resolution is 12 bits [15].

New hyperspectral missions such as PRISMA may increase the possibilities of innovative applications [13]. In fact, PRISMA data have already been used for detecting and classifying non-photosynthetic vegetation [16]; geological applications [17]; methane emission point mapping [18]; forest type discrimination [19]; fire fuel detection [20]; crop type mapping [21]; crop trait identification [22]; and local climate zone mapping [23].

However, hyperspectral data present its own challenges. The high dimensionality of HSI [24] requires a significant number of ground truths (GTs) to maintain the accuracy of the classifier [25,26]. While band selection or feature extraction techniques can help handle data dimensionality [27,28], GT availability remains a challenge, especially in developing countries as well as in areas with limited access. Furthermore, GT collection is a costly and time-consuming process. Common personal devices such as smartphones or tablets can facilitate data collection by a range of expert and non-expert users including professionals, scientists, or citizen scientists [29,30]. New user interfaces and applications facilitate contributions and simplify field surveys, expanding the amount of information and geotagged photos that can be used as reference data with appropriate pre-processing [31,32].

In this framework, innovative EO programs should be considered together with innovative data collecting and processing technologies including artificial intelligence (AI) [33]. Both EO and AI techniques can significantly contribute to developing databases for decision support systems. In the last decade, there has been a renaissance of deep learning (DL) models, especially due to advancements in computer technology and improvements in image analysis [34]. Before the advent of deep learning models, neural networks were overlooked in favor of traditional machine learning (ML) algorithms [34]. The development of new AI algorithms has expanded the range of available classification techniques, allowing for extremely accurate LU and LC classification [35]. Traditional ML algorithms have proven to typically not be well-suited for hyperspectral data and are being replaced by DL models [33]. The latter have shown great potential for the automatic learning of nonlinear data features that are difficult to detect through human analysis [33,36–38]. Some of the most widely used DL models are convolutional neural networks (CNNs) due to their architecture, which is particularly suited to hyperspectral data processing [34,39]. CNN models have demonstrated impressive accuracy in previous studies related to tree species classification [38–40].

The use of satellite RS data for tree species classification has increased exponentially since 2005/2010, partly due to the availability of LiDAR and hyperspectral data [41]. The majority of these studies have been based on different types of data: passive optical multispectral or hyperspectral data; LiDAR; SAR; or the results of data fusion from different sources [41,42]. Recently, Blickensdörfer et al. [43] demonstrated that predominant tree species can be mapped on a national scale using a combination of Sentinel-1 and Sentinel-2 time series. Dal Ponte et al. [44] combined high spatial resolution airborne hyperspectral data with multispectral satellite data and LiDAR to demonstrate that hyperspectral data provided the best results for classifying individual tree species in the southern Alps. Better discrimination of forest types using hyperspectral data was also shown in Vengi et al. [19] by comparing the PRISMA and Sentinel 2 spectral separability metrics.

Considering these recent advancements, the aim of this study was to explore the applicability of PRISMA hyperspectral satellite data for tree species classification in a forest environment. One of the aims of the PRISMA mission is to test the hyperspectral data

contribution in forest analysis and management [45]. To the best of our knowledge, no study has ever used PRISMA data to map land cover at the tree species level in a forest environment. Thus, the main novelty of this study lies in using spaceborne hyperspectral data in a forest context to distinguish forest classes based on predominant tree species. The investigation was conducted in a biodiversity-rich study area with different vegetation patterns where GSD could be a crucial factor.

Within this framework, the creation of labeled pixel datasets using GTs collected via smartphone apps (QField [46] and EyeLand [47]) was also explored. This allowed the suitability of these data collection instruments to be tested for classifier training. Artificial intelligence-based classification techniques were applied in this study to classify the forest category according to the predominant tree species. Considering the model performance in our previous LC classification study [48], a CNN was used to classify the PRISMA satellite data. While other models could be used, ML models have been shown to be less effective than DL models [33,34,48]. Given that this study was not focused on innovating classification techniques, an established CNN model [49] was selected from the range of available DL models.

Specifically, the study's objective was to address the following research questions:

- First, is it possible to achieve a detailed classification at the forest category level, defined according to the Third Italian National Forest Inventory (N.I.) [50], using PRISMA HSI, which coincides in some cases with individual tree species?
- Second, are the PRISMA data, with a GSD of 30 m, sufficient for the classification of forest trees in a context of high biodiversity and what accuracy level can be achieved with a single HSI?

2. Materials and Methods

2.1. Study Area

The study area, shown in Figure 1, is in southern Italy. The region of interest (ROI) is a square of about 441 km^2 and includes the Serre Regional Natural Park [51] (excluding Lake Angitola), which covers an area of 17,700 Ha.

The study area is crossed by the Apennine Mountains and has an elevation between 800 m and 1400 m above sea level. According to the Köppen–Geiger classification [52], the area's climate is classified as hot-summer Mediterranean (Csa) and partially as cool-summer Mediterranean (Csb) [52,53]. The importance of the study area is also related to its latitude (about 38°N), which is extremely southern for the Csb climate. In fact, the site experiences an anomalously high rainfall for southern Italian climates; at the meteorological station of Mongiana, located at the center of the study area, the average rainfall is about 1600 mm per year [54]. As a result, forest growth has always been intense. Historically, the practice of selective logging has contributed to the mixed cover of some areas [55,56]. Other studies [43] have shown that the combination of satellite imagery with environmental and climatic variables is useful for the classification of tree species on a large scale (e.g., national scale). However, in cases referring to smaller regions, the combination of satellite data with environmental variables has not necessarily led to significant increases in classification accuracy [57]. In this proposed case study, the study area corresponding to the PRISMA acquisition (900 km^2) was relatively limited. Therefore, climatic or environmental factors were not considered significant sources of enough internal variability within individual species to affect the spectral signature of each pixel. Furthermore, collecting many GTs for the same class in different regions of the image preserves the spectral variability representation within that same class, as shown below.

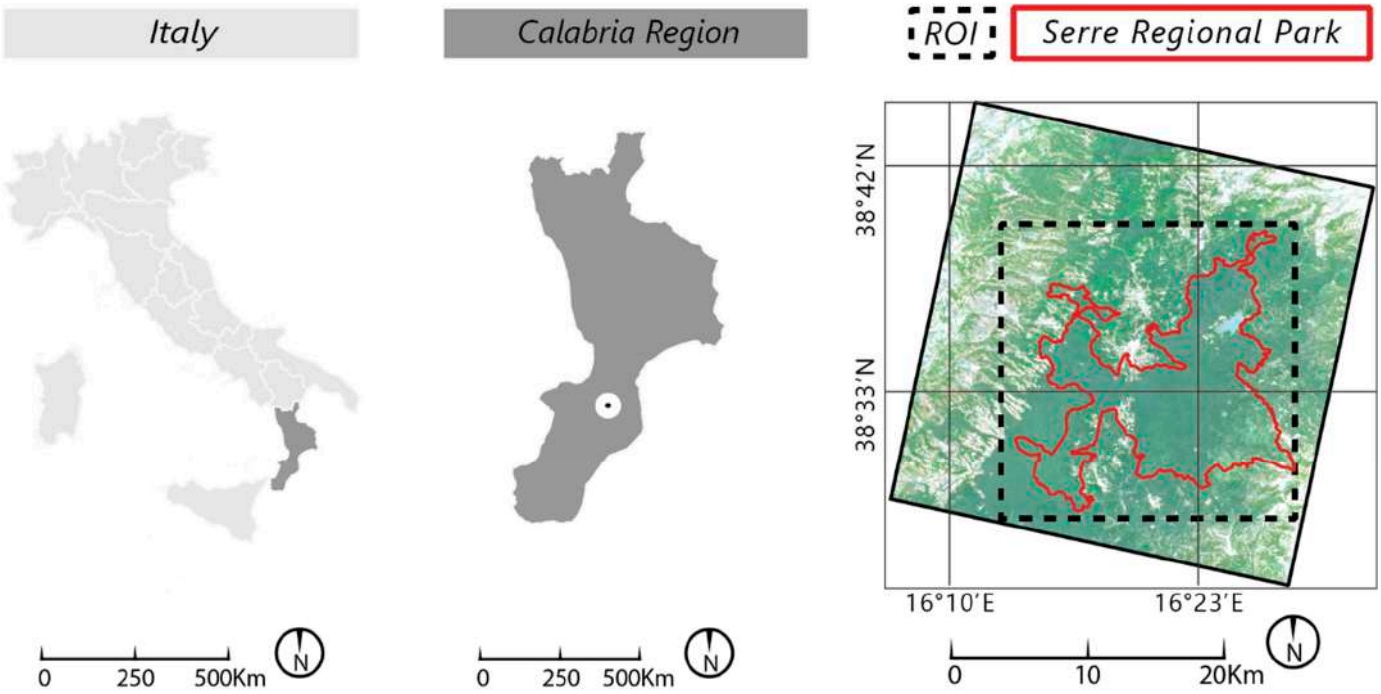

Figure 1. Framing of the study area. Authors' elaboration.

The study area contains the following Special Areas of Conservation (SACs) [58]: SAC IT9350121; SAC IT9340118; SAC IT9340119; SAC IT9340120. These areas were included in or partially overlapped the park area, as shown in Figure 2.

The Park Authority provided some GIS layers related to the SAC's classification (Table 1). These data were useful for determining the number and predominance of forest types as well as their spatial distribution (Figure 3).

Table 1. Dominant LC classes in hectares per SAC. Authors' elaboration.

	SAC IT9350121	SAC IT9340118	SAC IT9340119	SAC IT9340120	Tot. Class Area
Mixed areas (*Fagus sylvatica* and *Abies alba*)	3122	167	915	5	4209
Abies alba	1241	559	3	11	1814
Mixed areas (*Pinus nigra* and other conifers)		29	485	1	514
Castanea sativa	8	32	143		183
Quercus ilex	182				182
Pinus nigra	120	14		46	180
Areas with shrubs and herbaceous vegetation	24			75	99
Mixed areas (*Alnus glutinosa*, *Salix alba*, *Fraxinus excelsior*)		2		6	8
Fagus sylvatica	1				1
Alnus glutinosa		1			1
Total SAC area	4697	803	1546	143	

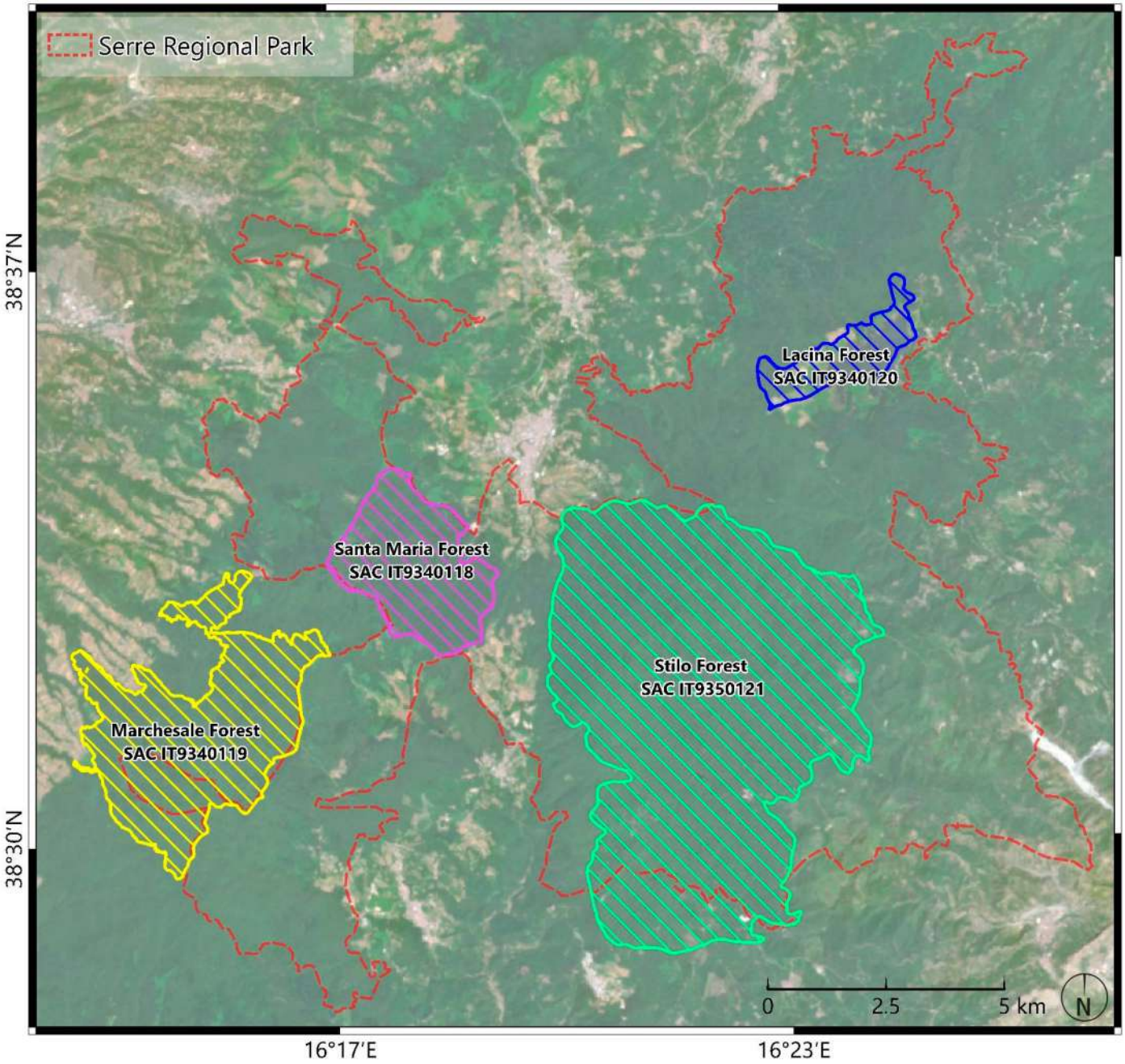

Figure 2. SACs areas included in the ROI. Authors' elaboration.

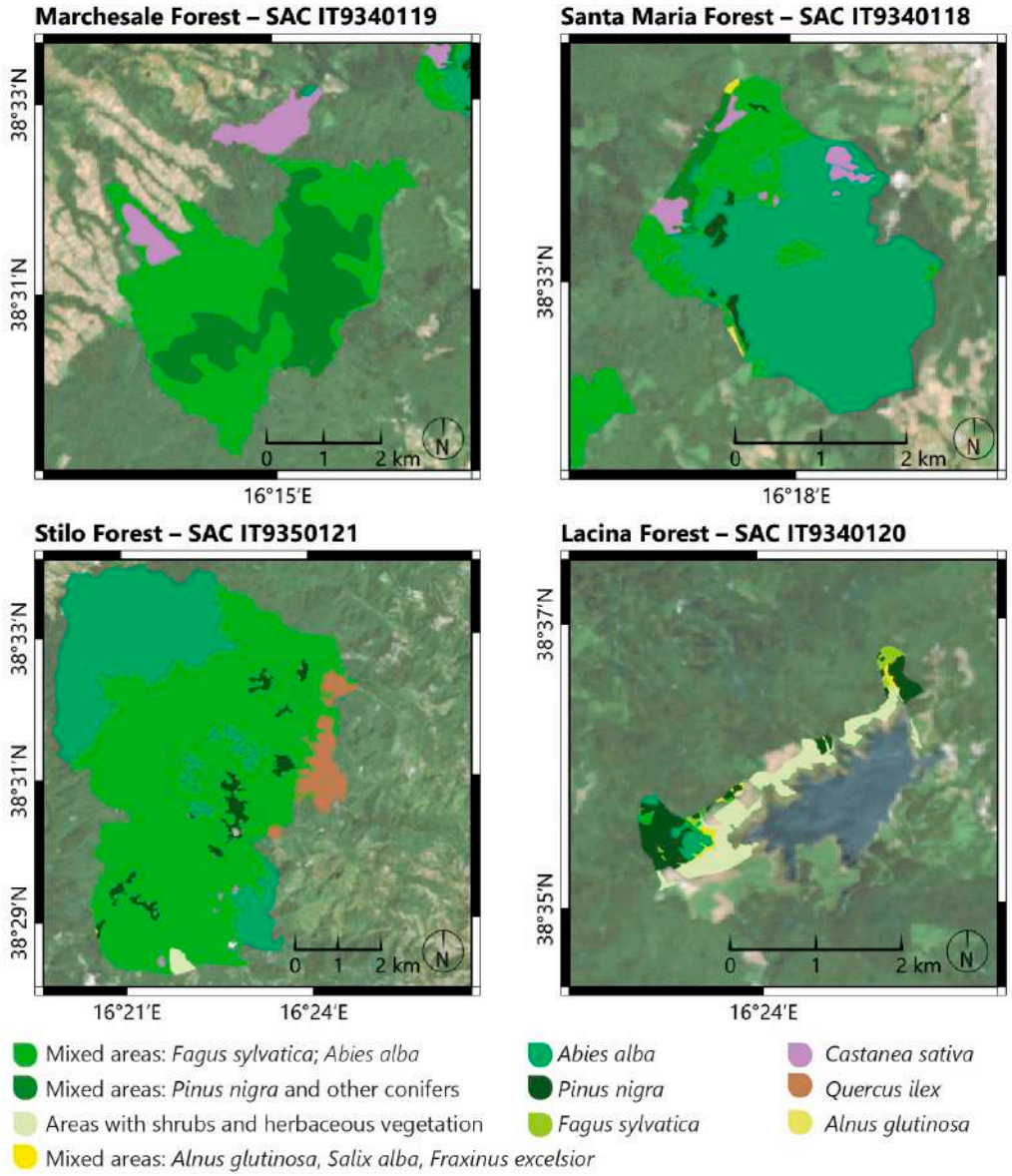

Figure 3. SAC forest type classification maps. Authors' elaboration.

2.2. Ground Truths

Data collected in the field were used to train the classifiers and test the final results to ensure validity between the classification results and the real world. While the SAC classification map could have served as a reference dataset from which to derive the baseline truths for the classification process, the presence of many mixed classification areas made it unsuitable for the purpose of this study.

Instead, a field survey to collect GTs was conducted in March 2024. The survey was carried out with the assistance of the Park Authority, which helped to identify the tree species, particularly during a period when some species had dropped their leaves. EyeLand [47] and Qfield [46] smartphone applications and the Geomax Zenith35 GNSS instrument were used to collect the field data. The EyeLand app was developed to facilitate GT point collection by non-expert users [47], but in this pilot application, it was tested by the authors for ease of use without exploring a citizen science element. The accuracy of the GNSS position from smartphones, which always have a horizontal range of less than 5 or 7 m, was considered acceptable given the 30-m GSD of the PRISMA image.

The field survey guidelines of the N.I. [50] were used to organize the GT dataset. The species were grouped as shown in Table 2. The classes chosen in this study are indicated in

the column "GT classes used". Category names were also included as metadata to provide information on the individual tree species as well as information on the surrounding habitat.

Table 2. Class definitions to generate the label dataset. Authors' elaboration.

N.I. Macro Category	N.I. Code	N.I. Category	GT Class Used	SAC Class
Conifer forest	03	Silver fir forest	Fir forest	*Abies alba*
	05	Black pine, larch, and loricate pine forest	Pine forest	*Pinus nigra*
Deciduous broadleaf forest	08	Beech forest	Beech forest	*Fagus sylvatica*
	11	Chestnut forest	Chestnut forest	*Castanea sativa*
	13	Hygrophilous forest	Hygrophilous species	*Fraxinus excelsior*
				Alnus glutinosa
				Salix alba
Evergreen broadleaf forest	15	Holm oak forest	Holm oak forest	*Quercus ilex*
Shrubland, maquis	23	Maquis, Mediterranean shrubland	Grassland and shrubs	Area with shrubs and herbaceous vegetation

A total of 784 plots with an estimated minimum area of 30 × 30 m (PRISMA GSD) were collected in the field, resulting in a first dataset of labeled data (DS_1). DS_1 contained a total of 766 labeled pixels. The number of plots exceeded the number of pixels because multiple plots collected by different users were contained within the same pixel (900 m^2) in a few cases. Additional information recorded during the survey included an evaluation of canopy cover homogeneity outside the plot area. This evaluation was conducted within a variable radius that depended on the degree of canopy cover homogeneity, averaging about 100 m. This information was useful during postprocessing to label additional pixels, adjacent to those contained in DS_1, according to the information on the canopy cover homogeneity outside the plot area. In this way, it was possible to generate a second dataset with an additional 1865 labeled pixels (DS_2) using the information collected during the survey and through photointerpretation using the Google basemap in the Qgis software (version 3.34) [59]. Figure 4 shows the distribution by class of the labeled pixels belonging to DS_1 and DS_2. It should be noted that only the plots belonging to DS_1, collected in the field, were used to test the final result in this study, ensuring greater scientific reliability.

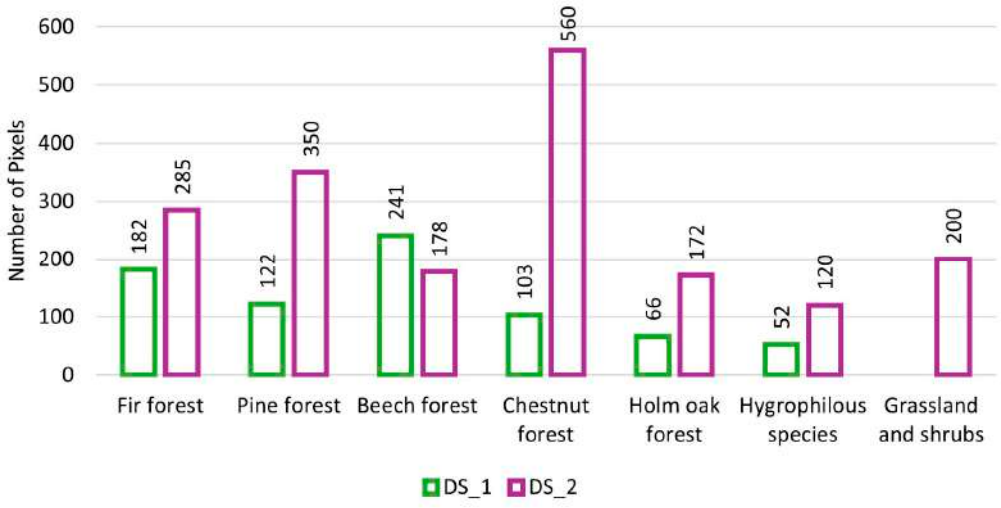

Figure 4. Labeled dataset. DS_1 indicates the labeled pixels corresponding to the plots collected in the field. DS_2 indicates the labeled pixels derived from the information collected in the field as well as from the photointerpretation. Authors' elaboration.

The "Grassland and shrubs" class deserves special mention. For this class, no field plots were collected. As grasslands are easily distinguishable, photointerpretation in Qgis was used to obtain the 200 pixels belonging to this class in DS_2.

2.3. Data Mining

This study used an HSI acquired by the PRISMA hyperspectral satellite on 25 July 2023. This was at the L2D level, the geocoded version of the L2C that is geolocated at bottom-of-atmosphere reflectance [60]. LD2 images are atmospherically corrected and orthorectified by the Italian Space Agency [60]. The PRISMA L2D level cube, provided in HDF5 format, was converted to GeoTiff format using a Python application developed by the authors and is available for download [61]. The same Python script was used to improve the georeferencing of the images by inserting the coordinates of the four scene vertices. This process resulted in the extraction of the original cube (Cube_O) with 234 bands. Cube_O was then subsetted to the ROI. This made it possible to include all of the polygons of the SAC areas (Figure 2) including those that lay partially outside the park boundary. Subsetting Cube_O produced Cube_S. To identify bands with missing information, an analysis of the pixel value distribution in Cube_S was performed using R software (version 4.3.0) to detect bad bands [62]. These bands mostly corresponded to windows of the electromagnetic spectrum with zero transmittance values, associated with atmospheric noise [63]. A new cube (Cube_R1) was obtained after removing the bands highlighted in Figure 5 in the following ranges: bands from 104 to 112 (1361.0 nm to 1449.1 nm); bands from 147 to 163 (1803.5 nm to 1949.9 nm); bands from 232 to 234 (2483.7 nm to 2497.1 nm). Finally, the new Cube_R1 consisted of 205 bands.

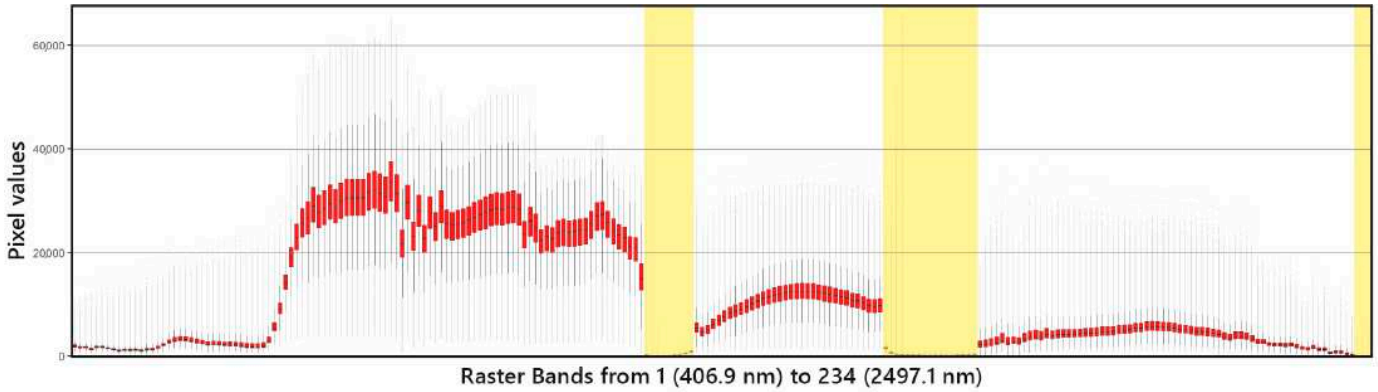

Figure 5. Distribution of the pixel digital numbers corresponding to the reflectance values. The graph shows the box plots for each of the 234 PRISMA data bands in red. The yellow highlighted areas correspond to regions where bands were removed. Authors' elaboration.

Since classifiers and their results are known to be affected by data normalization and how it is performed, Cao et al. [64] suggested using the "band min–max" method for HSI classification. Therefore, using R software, Cube_R1 was normalized to obtain Cube_R1_N (normalized).

For the next steps, the pixels corresponding to the vegetated areas were isolated, and everything else was excluded. In order to do this, the normalized difference vegetation index (NDVI) was used, as it is a popular choice [65] for vegetation assessment. Several vegetation indices have been defined in the literature using both multispectral or hyperspectral data [66,67]. Hyperspectral data, unlike multispectral data, have a series of narrow bands in both the red and infrared spectral regions. The NDVI was calculated following Haboudane et al. [66] using Formula (1), where R_x is the reflectance at a given wavelength (nm).

$$\text{NDVI} = \frac{(R_{806} - R_{664})}{(R_{806} + R_{664})} \quad (1)$$

The NDVI value distribution for pixels overlaid with ground truth datasets (DS_1 and DS_2) was examined to identify the pixels to be preserved. The median NDVI values were all above 0.6, as shown in Figure 6. However, in some cases, the values were lower considering outliers. Therefore, as a precaution, we decided to keep all pixels with an NDVI greater than 0.4, also considering the thresholds for different LC types reported by Mehta, Shukla, and Rakholia [68]. A mask was applied to Cube_R1_N, creating Cube_R1_M (mask), to only preserve the regions with values above this threshold. This step considered the areas of vegetation that were present at the time of the image acquisition (25 July 2023).

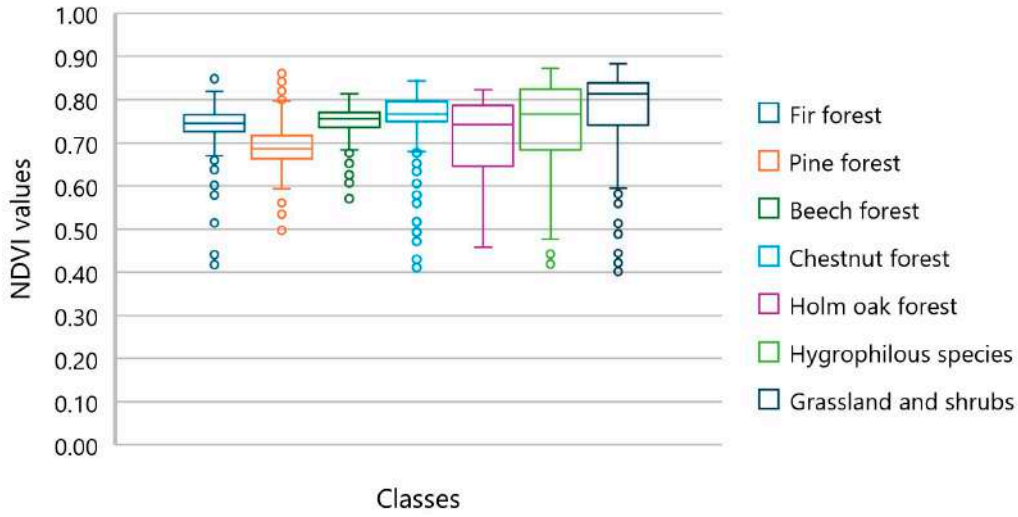

Figure 6. NDVI distribution by class of labeled pixels from the GT database. Authors' elaboration.

Using hyperspectral data can be very challenging due to the large amount of information available and the time-consuming process required [35,36]. Indeed, another process at this stage involves reducing the data's dimensionality to deal with the Hughes phenomenon [24]. Nevertheless, having many bands can improve the ability to discriminate between similar entities [36]. Techniques for dimensionality reduction can be broadly classified into two categories: feature extraction and band selection. Methods based on feature extraction, such as principal component analysis (PCA), select a subset of features with a high variance from the original dataset [69]. However, these methods may result in information loss. Consequently, the band selection method is often favored when dealing with HSIs [70], as this technique involves the selection of a subset of bands without compromising their physical interpretation [71,72].

In this study, three different banded HSIs were tested to evaluate the impact that the available spectral information might have on the accuracy of the results. Cube_R1_M with 205 bands was used in the first set of experiments. In this case, the band selection only involved removing the bands without information. The other two sets of experiments were performed with HSIs obtained through PCA. Considering the same number of principal components, the cumulative variance increased less rapidly for Cube_R1 than for Cube_R1_M, which only contained vegetated areas, as shown in Figure 7. For the first set, 30 principal components were selected. This made it possible to obtain Cube_R2_M and preserve 99.9% of the data variance. For the second set, 16 principal components were selected to evaluate the effect of halving the components while preserving a high percentage of variance. This resulted in Cube_R3_M, which retained 99.8% of the data variance.

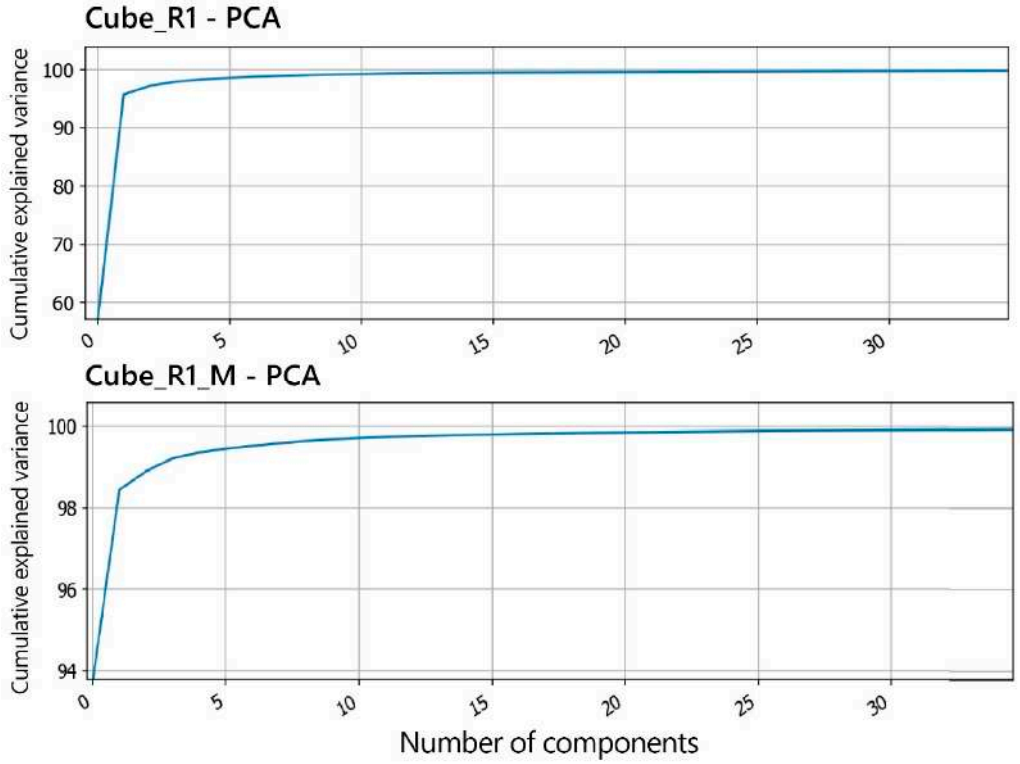

Figure 7. PCA of Cube_R1 and Cube_R1_M. This graph shows the growth of the cumulative variance as the components increase.

2.4. Classification Task

The remote sensing community is constantly investigating classification models that improve the accuracy of results. Prior to the development of deep learning models, neural networks were underutilized in favor of traditional machine learning algorithms such as random forest (RF) or support vector machine (SVM) [34]. For HSI classification, previous studies have shown that DL models generally outperform ML models [33,37,38,48]. As the focus of this paper was on an applied case study and not on a comparative analysis of classification models, we decided to use a DL model, taking into account the results of our previous study with PRISMA data [48,73]. In this study, the AVHYAS plugin [74], available in the open-source software Qgis, was used for the classification task. A CNN was used, since their architecture is particularly suited to processing large datasets such as hyperspectral cubes [34]. Specifically, the CNN model proposed by Hu et al. [49] was selected. This model is composed of five layers: first, there is the input layer, represented by a pixel spectral vector, followed by the convolutional layer, the max pooling layer, the full connection layer, and finally, the output layer. The model was based on the spectral signature and does not consider spatial information. It was chosen because the spectral signature shape may be more relevant for class recognition than textures, patterns, or boundaries when using the PRISMA HSI with a 30 m GSD.

The classification was carried out for a total of 15 experiments, with 5 tests for each of the input datasets. The variations between the five tests for each input data cube were related to the selection of different labeled pixels stored in DS_1 and DS_2. The same percentage of random partitioning of DS_1 and DS_2 was used for each of the selections (Sel_1; Sel_2; Sel_3; Sel_4; Sel_5). Specifically, depending on the number of labeled pixels available for each class in DS_1, the selection percentage for test dataset creation varied: 40% was used to randomly select pixels for those classes with more than 100 labeled pixels, while the remaining 60% was merged with DS_2 to train and validate the model. For classes with less than 100 labeled pixels, the percentage for testing was increased to 80%, and 20% were merged with DS_2 for model training and validation. Thus, only the labeled

pixels belonging to DS_1 were used to test the final map. The data from DS_1 that were not selected for testing were added to DS_2 data and used to train the network and validate the model performance. In particular, 70% of the data were randomly selected for training and 30% for model performance validation for all classes. Then, to reduce the dependence of the results on the specific selection of each experiment, a 5-fold selection was used, where a random selection of training, validation, and test pixels was repeated five times. The labeled pixels used at the end of each of the five random selections for training, validation, and testing are shown in Figure 8. These percentages were chosen based on what is commonly used in the literature [75]. The possibility of reducing or increasing the number of labeled pixels used for the training, validation, or testing phases was not considered, given the good results obtained. Rather than testing the performance of the classification model, the usability of the PRISMA data to discriminate tree species was the main aim of this work.

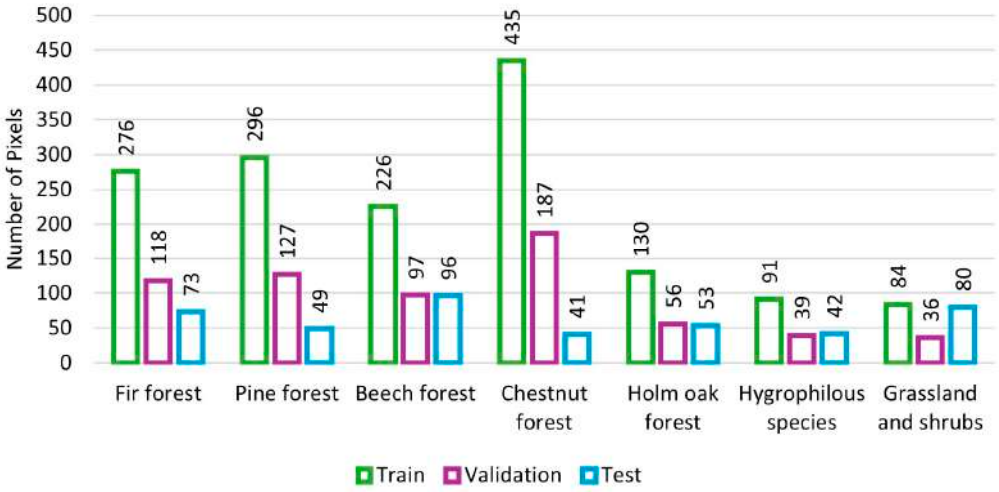

Figure 8. This graph shows the pixels used for training, validation, and testing in each of the five random selections. Authors' elaboration.

Regarding the setting parameters of the chosen CNN model, an initial number of 200 epochs and a learning rate of 0.001 was used in all experiments, as these are the most common in the literature [76]. A number of experiments were carried out to test these values on the datasets used before choosing the values given above. An increase (0.01) or decrease (0.0001) in the learning rate resulted in lower accuracy (0.87 and 0.82, respectively) and higher loss (0.41 and 0.55, respectively). An increase (300) or decrease (100) in number of epochs resulted in lower accuracy (0.91 and 0.85, respectively) and higher loss (0.27 and 0.44, respectively). Based on these results, we decided to set the initial epochs to 200 and the learning rate to 0.001, since these values gave higher accuracy and lower loss in all experiments. The other AVHYAS plugin settings remained at their default values. As shown in Table 3, the model automatically stopped training early to avoid overfitting, resulting in a lower number of epochs in some experiments. Only the experiments with an accuracy above 0.9 and a loss below 0.2 were retained. The time required to classify the HSI (CNN training and validation) never exceeded 10 minutes (the tests were performed on an HP laptop with an AMD Ryzen 7 PRO 7840HS processor, a Radeon 780 M graphics card, 3.80 GHz, and 32.0 GB RAM).

Table 3. This table reports the CNN input data and shows the number of epochs, accuracy, and loss of the CNN used for each test. Authors' elaboration.

Input	n. Test/Sel	n. Epochs	Accuracy	Loss
Cube_R1_M	1	165	0.955	0.145
	2	200	0.946	0.183
	3	152	0.946	0.177
	4	184	0.949	0.178
	5	200	0.945	0.171
Cube_R2_M	1	184	0.964	0.105
	2	200	0.963	0.111
	3	174	0.968	0.097
	4	188	0.966	0.114
	5	200	0.966	0.106
Cube_R3_M	1	200	0.972	0.089
	2	193	0.973	0.096
	3	200	0.950	0.137
	4	161	0.954	0.137
	5	195	0.969	0.124

Finally, the model was validated and the final classification map was tested. The metrics used in the statistical analyses of the accuracy evaluation were: overall accuracy (OA), Kappa coefficient (K), user accuracy (UA), and producer accuracy (PA) [29,77], along with the F1 score (F1), which is the harmonic mean of precision and recall and is another metric measured for each class [78]. It is useful for unbalanced datasets and ranges from 0 (worst) to 1 (best) [79]. The results related to the model validation were automatically generated by the AVHYAS plugin. The results related to the final testing phase were generated using the SCP plugin [80] using the DS_1 GTs collected in the field.

3. Results

This section reports the results for the metrics used, calculated using the error matrices. All metrics are available in the Supplementary Materials (Table S1: Model_Validation_Test). Two matrices were generated for each test of the 15 experiments. The first was to validate the model and the second was to test the final map. In the following tables, the arithmetic mean (average) was added for each input as it is considered to be more representative than a single test (single selection of labeled pixels), and was calculated over the five results obtained from the five selections.

The following tables show the accuracy values obtained in all of the experiments. The scores relate to both the validation of the performance of the classification model and the testing of the final classification map. Table 4 shows the overall results in terms of OA, K coefficient, and F1 for each test. In the case of the validation phase, the highest OA was obtained using Cube_R1_M. Cube_R1_M also had a marginally higher K coefficient, while Cube_R2_M produced a slightly higher F1 value. Regarding the test results, the highest OA, both as a single test and considering the average value, was obtained using Cube_R2_M. Cube_R2_M also provided the highest K coefficient and F1 value.

Table 5 shows the results in terms of the F1 for each individual class. The mean value is calculated for each of the five labeled pixel selections. The values in the table refer to both the validation (first number) and the map's test (second number) and are separated by a semicolon.

Table 4. Validation and test results in terms of OA, K, and F1 for each test. Authors' elaboration.

			VALIDATION			TEST		
Input	**n. Test**	**GT**	**OA**	**K**	**F1**	**OA**	**K**	**F1**
Cube_R1_M	Test_1	Sel_1	0.943	0.932	0.928	0.899	0.874	0.820
	Test_2	Sel_2	0.928	0.915	0.922	0.869	0.837	0.773
	Test_3	Sel_3	0.936	0.924	0.923	0.892	0.866	0.817
	Test_4	Sel_4	0.920	0.905	0.907	0.859	0.825	0.747
	Test_5	Sel_5	0.907	0.890	0.887	0.865	0.833	0.758
	Average		**0.927**	**0.913**	**0.913**	**0.876**	**0.847**	**0.783**
Cube_R2_M	Test_6	Sel_1	0.920	0.905	0.914	0.910	0.889	0.842
	Test_7	Sel_2	0.914	0.897	0.906	0.861	0.829	0.765
	Test_8	Sel_3	0.935	0.922	0.930	0.892	0.866	0.813
	Test_9	Sel_4	0.921	0.907	0.912	0.889	0.862	0.800
	Test_10	Sel_5	0.931	0.918	0.929	0.899	0.875	0.821
	Average		**0.924**	**0.910**	**0.918**	**0.890**	**0.864**	**0.808**
Cube_R3_M	Test_11	Sel_1	0.915	0.900	0.910	0.903	0.880	0.832
	Test_12	Sel_2	0.914	0.898	0.898	0.890	0.863	0.810
	Test_13	Sel_3	0.925	0.911	0.919	0.869	0.838	0.776
	Test_14	Sel_4	0.932	0.919	0.932	0.880	0.851	0.787
	Test_15	Sel_5	0.928	0.915	0.917	0.883	0.855	0.798
	Average		**0.923**	**0.908**	**0.915**	**0.885**	**0.858**	**0.800**

Considering the validation results, the best performance was obtained for the "Chestnut forest" class (0.96) using the Cube_R1_M. Results above 0.90 were also obtained for "Beech forest" and "Grassland and Shrubs", regardless of the input data. The lowest model performance with both Cube_R1_M and Cube_R3_M was recorded for the mixed class "Hygrophilous species" (0.82). For the other classes, the CNN used achieved an average F1 ranging from 0.80 to 0.90.

In the case of the test results, considering the average value, the best accuracy in map classification testing among the tree species was obtained for the class "Beech forest" (0.90) using Cube_R2_M. Using the same dataset as input, results above 0.8 were obtained for the classes "Fir forest" (0.81) and "Holm oak forest" (0.82), while the "Pine forest" (0.78) class obtained a slightly lower F1. The lowest F1, regardless of the input data, was recorded for the mixed class "Hygrophilous species" (0.65) using Cube_R1_M and for the class "Chestnut forest" (0.67) using Cube_R3_M.

Figure 9 shows the distribution of the F1 values obtained by each of the classes in the fifteen trials in the validation phase. The classes with the largest ranges between the minimum and maximum values were the mixed class "Hygrophilous species" (0.17), "Holm oak forest" (0.17), and "Grassland and shrubs" (0.12). The rest of the classes showed less sensitivity to the HSI image used as input and/or to the selection of labeled pixels used for training and validation.

Figure 10 shows the distribution of F1 values obtained by each class using the three different inputs in the test phase. The highest differences between the minimum and maximum values were recorded with Cube_R1_M. The classes with the largest ranges were "Holm oak forest" (0.26) and "Hygrophilous species" (0.19). The latter also showed a relatively large interval (0.14), as did the "Pine forest" class (0.13) when using Cube_R2_M. Using Cube_R3_M, the class with the largest interval was "Chestnut forest", which also had about the same interval when the other two HSIs were used as input. The other classes

showed less sensitivity to the HSI image used as input and/or to the selection of the labeled pixels used to test the results.

Table 5. F1 obtained for each individual class in each test. Values refer to both the validation (first number) and final classification map test (second number). Validation and test F1 scores are separated by a semicolon. Authors' elaboration.

	Sel_1	Sel_2	Sel_3	Sel_4	Sel_5	*Average*
			Cube_R1_M			
Fir forest	0.91; 0.85	0.87; 0.77	0.90; 0.81	0.88; 0.80	0.86; 0.81	**0.89; 0.81**
Pine forest	0.93; 0.80	0.90; 0.75	0.90; 0.80	0.90; 0.75	0.85; 0.75	**0.90; 0.77**
Beech forest	0.95; 0.92	0.92; 0.84	0.95; 0.90	0.92; 0.87	0.93; 0.89	**0.93; 0.88**
Chestnut forest	0.95; 0.75	0.96; 0.69	0.97; 0.73	0.95; 0.63	0.97; 0.70	**0.96; 0.70**
Holm oak forest	0.92; 0.74	0.90; 0.78	0.91; 0.84	0.87; 0.72	0.80; 0.58	**0.88; 0.73**
Hygrophilous species	0.85; 0.73	0.86; 0.63	0.85; 0.73	0.78; 0.54	0.75; 0.64	**0.82; 0.65**
Grassland and shrubs	0.99; 0.95	0.96; 0.94	0.91; 0.91	0.96; 0.92	0.93; 0.95	**0.95; 0.93**
			Cube_R2_M			
Fir forest	0.85; 0.81	0.85; 0.75	0.89; 0.81	0.88; 0.84	0.87; 0.83	**0.87; 0.81**
Pine forest	0.88; 0.84	0.86; 0.71	0.90; 0.78	0.87; 0.79	0.91; 0.80	**0.88; 0.78**
Beech forest	0.94; 0.95	0.95; 0.86	0.94; 0.88	0.94; 0.92	0.96; 0.90	**0.95; 0.90**
Chestnut forest	0.95; 0.74	0.94; 0.63	0.97; 0.72	0.95; 0.65	0.95; 0.64	**0.95; 0.68**
Holm oak forest	0.93; 0.84	0.92; 0.79	0.89; 0.82	0.91; 0.81	0.90; 0.82	**0.91; 0.82**
Hygrophilous species	0.81; 0.76	0.79; 0.66	0.89; 0.71	0.86; 0.66	0.88; 0.80	**0.84; 0.72**
Grassland and shrubs	0.96; 0.96	0.94; 0.95	0.97; 0.96	0.88; 0.92	0.97; 0.97	**0.95; 0.95**
			Cube_R3_M			
Fir forest	0.87; 0.80	0.88; 0.76	0.87; 0.75	0.86; 0.81	0.89; 0.78	**0.87; 0.78**
Pine forest	0.89; 0.82	0.90; 0.80	0.89; 0.76	0.89; 0.77	0.92; 0.79	**0.90; 0.79**
Beech forest	0.92; 0.91	0.92; 0.90	0.98; 0.90	0.96; 0.92	0.95; 0.88	**0.95; 0.90**
Chestnut forest	0.93; 0.74	0.93; 0.71	0.94; 0.62	0.95; 0.63	0.94; 0.65	**0.94; 0.67**
Holm oak forest	0.89; 0.82	0.92; 0.86	0.90; 0.78	0.97; 0.79	0.90; 0.81	**0.92; 0.81**
Hygrophilous species	0.82; 0.75	0.72; 0.69	0.82; 0.70	0.86; 0.66	0.87; 0.71	**0.82; 0.70**
Grassland and shrubs	0.96; 0.97	0.90; 0.95	0.96; 0.92	0.97; 0.93	0.87; 0.97	**0.93; 0.95**

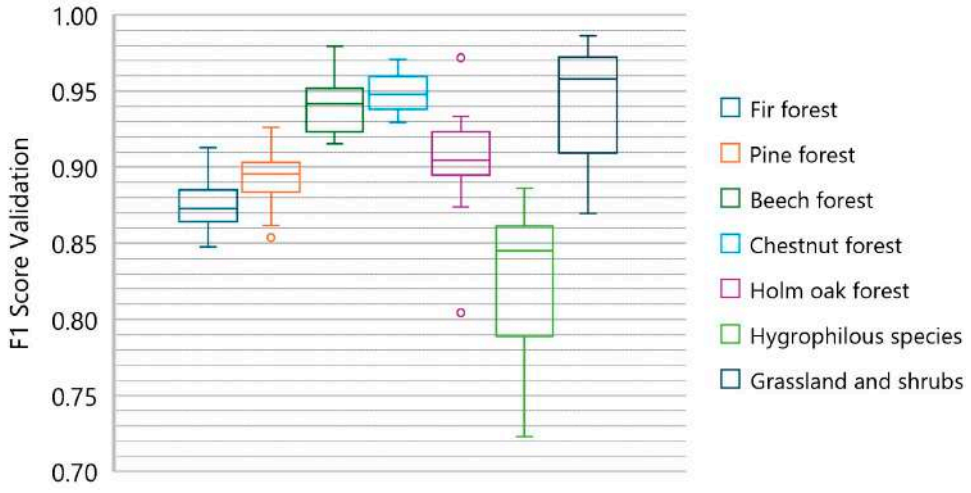

Figure 9. F1 distribution by class considering all the experiments. Values refer to the validation phase. Authors' elaboration.

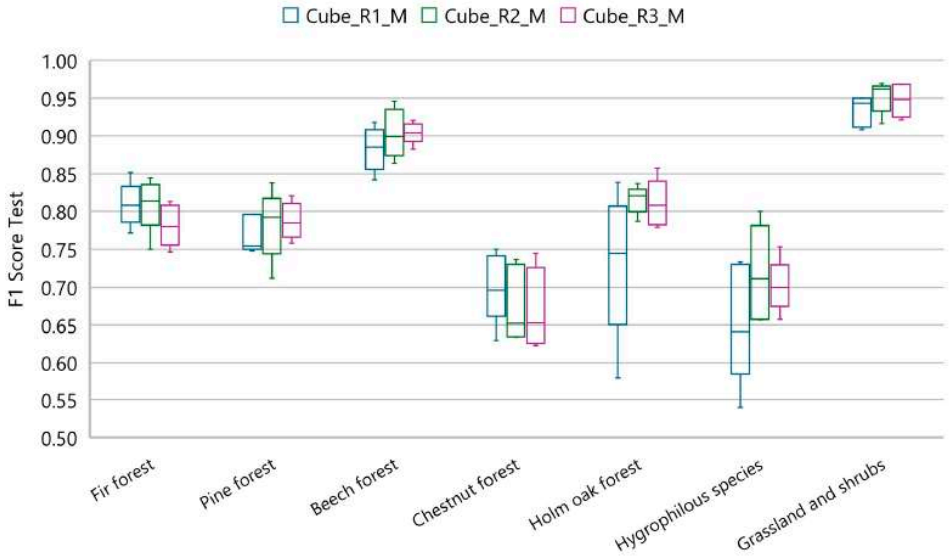

Figure 10. F1 scores by class, distinguished for each input cube. Values refer to the test phase. Authors' elaboration.

Figure 11 shows the map obtained with Test_1, which was the test with the optimal reliability regarding the final scores, considering all 15 tests performed. Even if there was a trade-off for some classes in light of the higher results obtained in the other tests, Test_1 offered the best overall balance considering the values obtained in terms of F1.

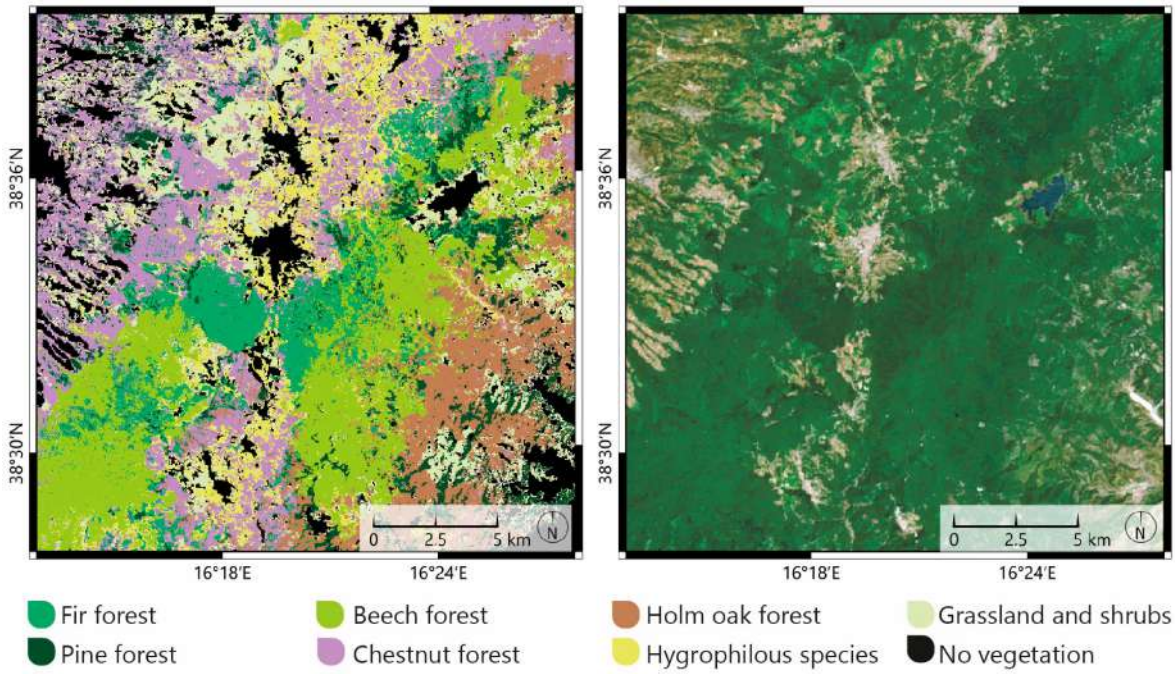

Figure 11. Classification map result from Test_1 on the left. PRISMA image in RGB composition on the right. Authors' elaboration.

Finally, the results obtained in this study were compared with the pre-existing SACs LC classification in order to analyze their convergences and divergences, even though the latter contains more areas of mixed cover than polygons assigned to pure classes. The two classifications were overlaid and the class correspondences shown in Table 2 were used for the comparison. Figure 12 shows the results obtained in Test_1 within the perimeter of the SACs. Figure 13 shows what the composition of the SAC classes would be on the basis of the results of this study.

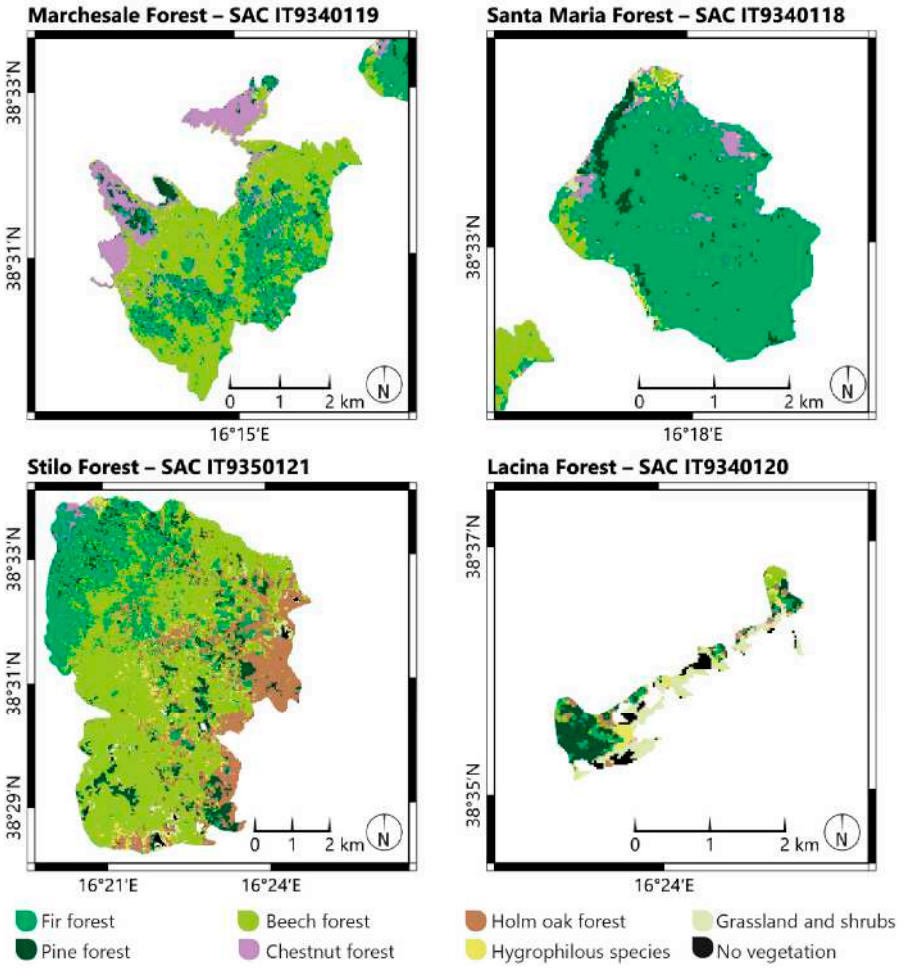

Figure 12. Classification results obtained in Test_1 within the perimeter of the SACs. Authors' elaboration.

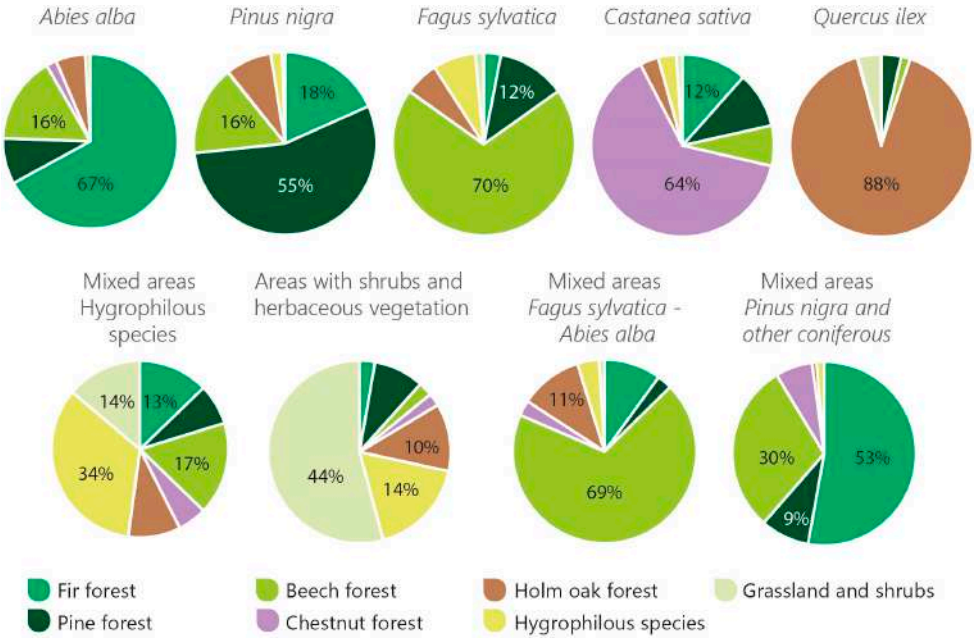

Figure 13. Composition of the SAC classes with respect to the results of this study (only the largest percentages are shown). Authors' elaboration.

4. Discussion

The results obtained in this study confirm that hyperspectral data strongly increase the ability to discriminate between similar entities in forest classifications, consistent with findings in previous studies [10,19,44,81]. Furthermore, the ability of DL models to handle HSI data [33,36,37] was demonstrated by the accuracy values obtained in the model validation of the CNN used [49,74]. The results showed rather high values for all accuracy metrics used, considering other studies aimed at using RS to classify tree species [41]. The case study results showed an average OA of 0.92 in the validation phase and an average OA of 0.88 in the test phase. The average K was 0.91 in the validation phase and 0.86 in the test phase, while the average F1 was 0.92 in the model validation phase and the average F1 of 0.80 in the test phase. For most of the classes considered, higher results were obtained (around 0.90 in terms of F1) when considered individually.

Fassnacht's review of tree species classification from RS data [41] discusses the concept of accuracy in classifying tree species. According to Floody et al. [82], the level of accuracy can depend on the needs of the user and the type of application. Some authors of reviewed papers [83–85] set an OA target for forest type mapping (80% in northwestern USA and 95% in Finland). Thomlinson et al. [86] set a minimum OA of 85% for land cover studies and a minimum of 70% for individual classes.

Since there are no similar studies on PRISMA data classification for tree species recognition using CNNs in forests, the results of this study could only be compared with similar studies regarding the satellite data used, the classification model used, or the object of classification. Rogers et al. [87] classified 21 land cover types using PRISMA data with an average balanced accuracy of 76% and an F1 of 77%. Vanguri et al. [88] classified tree species using EnMAP hyperspectral data combined with Sentinel using ML algorithms and achieved the best results in model validation with SVM with an average OA of 0.94 between the deciduous and coniferous LC. Dal Ponte et al. [44] obtained the best K accuracy (88%) in the validation of the classification of five forest types using SVM on a combination of 30 hyperspectral and LiDAR bands. Frickern et al. [89] achieved an average F1 of 0.87, classifying seven tree species using CNN and high spatial resolution airborne hyperspectral data. Comparing the accuracy achieved in this study with these previous forest classification studies demonstrated that using a single PRISMA HSI dataset could yield quite accurate classification results.

It is also interesting to compare the results obtained in this study with the classification of the SACs in order to analyze their convergences and divergences, even though the latter contained more areas of mixed cover than polygons assigned to pure classes. The predominant class in the PRISMA classification was the same as in the SAC classification in the homogeneous SAC polygons. Nevertheless, other classes with lower percentages were also included in these areas due to the higher level of detail in this study. In the mixed cover polygons, the SAC classification and the results of this study also agreed in terms of the prevalent species. An exception was the class "Mixed areas (*Pinus nigra* and other conifers)", where the dominant species in this study was "Fir forest" due to the class polygon extent and difficulty in distinguishing conifers in SAC classification.

As shown in [19], PRISMA's spatial resolution does not limit its application, and its spectral resolution makes it possible to discriminate between similar forest types. Indeed, it has been shown that hyperspectral data are less dependent on GSD [83], and high spatial resolution does not necessarily lead to more accurate results [90]. However, the GSD of PRISMA HSI deserves more attention, even though it appears to be effective in areas of mixed coverage. Spectral unmixing techniques seem very promising and may lead to a better interpretation of the spectral composition in the future [91].

There is not always a strong correlation between the accuracy values and the availability of labeled pixels as it depends on the class type and its spectral response. Classes with fewer samples, such as "Grassland and shrubs" and "Hygrophilous species", showed significant differences in F1 values because mixed classes have inherently inhomogeneous characteristics.

The very high accuracy values obtained may be an indication of possible overfitting, also in light of the size of DB_1 and DB_2. However, regardless of the labeled pixels selected for training, validation, and testing, the resulting accuracy values were nearly stable. This stability, together with the early arrest of the classification model in the training phase described in Section 2.4, prevented overfitting in the final classification. Even when considering cases where a decrease in accuracy was observed, the results remained consistent with values reported in other studies [42,81]. Nevertheless, a larger labeled dataset could result in less variation in accuracy across trials. When the statistical sample size is modest, a significant increase or decrease in accuracy may be more influenced by the labeled pixels used in the sample than by actual variations in the model predictions. Hyperspectral data are notorious for the large amount of sample data required, especially when DL models are used. In this study, the representativeness of the data for CNN training was enhanced by adding approximately 1800 additional labeled pixels (DS_2) from the smartphone app to the approximately 750 plots collected in the field. The additional dataset was added based on the information and photos collected with the smartphone app. This shows how personal devices can facilitate data collection by expert users and may indicate the potential of expanding its use to non-experts through citizen science.

An important consideration is that the results were based on a single image. It is likely that the results could be further improved with multitemporal analysis or by combining different sources (e.g., LiDAR). The wide availability of long time series of multispectral data remains a valuable tool. Recently, Blickensdörfer et al. [43] demonstrated that major forest species can be mapped using a combination of Sentinel-1 and Sentinel-2 time series. However, the potential of hyperspectral data seems to guarantee excellent results, even with limited acquisitions and in areas of mixed forest cover.

Optical sensors have been used to measure the aboveground biomass over large areas by linking reflectance variations to field measurements, however, canopy structural conditions can change more rapidly than a satellite temporal resolution can record [9]. In the case of hyperspectral missions such as PRISMA, this problem can be exacerbated by infrequent data acquisition [45]. An overview of the strengths and weaknesses of the PRISMA mission is reported in [45]. Some weak points are related to the difficulty in accessing data compared to the high number of requests and the long revisit time in the same area of ~16 days [45]. However, data fusion with high temporal resolution multispectral sensors such as Sentinel may provide a solution, combining the high spectral resolution of the original hyperspectral dataset with the temporal repeatability of multispectral data [92].

5. Conclusions

This paper explored the use of PRISMA data for forest classification and provides results confirming that: (1) a detailed classification at the forest category level can be obtained using PRISMA HIS and (2) the PRISMA data's GSD of 30 m is sufficient for the classification of forest trees in a context of high biodiversity and can achieve a high accuracy level with a single HSI. However, a higher accuracy was observed for pure cover with respect to mixed cover. This indicates that without additional processing, such as spectral unmixing, the classification of HSI with 30 m GSD is less effective in mixed cover cases. The study also dealt with the need for data dimensionality reduction. The best overall balance in accuracy validation and testing was achieved using the 205-band cube, but fewer bands can also yield high accuracy when fast processing is required. Finally, the paper demonstrated the potential of using smartphone apps to collect GTs. It should be noted, however, that the post-processing of such data is time consuming and requires a thorough verification of each labeled pixel.

This study was limited by the current scarce availability of hyperspectral data. There are few active hyperspectral satellites, and weather conditions often prevent regular acquisition. Indeed, the use of a single satellite image, rather than a time series or a combination of different sources, is certainly a limitation of this study. However, given the scarcity of data in certain regions, the possibilities offered by a single PRISMA image appear very

promising. Depending on the purpose of the study, a single image could provide sufficient accuracy without resorting to multitemporal analysis or data fusion. The imminent launch of further hyperspectral missions could also help to overcome the limited availability of hyperspectral satellites.

Possible directions for future research include the combination of PRISMA data with radar or higher resolution imagery and leveraging networks of field data collectors. The production of detailed land cover maps with HSI could enable tree species to be correlated with vegetation indices to measure vegetation health. Finally, it should be noted that the availability of current data, HSIs, and GTs will be extremely powerful in the future. For example, comparisons of the effects of climate change based on data collected in previous years will be possible in the future as scientific knowledge and more advanced technological processing tools become available.

Supplementary Materials: The following supporting information can be downloaded at: https://www.mdpi.com/article/10.3390/rs16244788/s1, Table S1: Model_Validation_Test.

Author Contributions: Conceptualization, G.D., F.R., M.N.R. and L.B.; Methodology, G.D., E.C., A.P., F.R., M.N.R. and L.B.; Software, G.D. and L.B.; Validation, G.D., A.P., C.C.F., F.R. and L.B.; Formal analysis, G.D.; Investigation, G.D. and L.B.; Resources, G.D., F.R., M.N.R. and L.B.; Data curation, G.D., M.P., E.C., A.P. and C.C.F.; Writing—original draft preparation, G.D. and L.B.; Writing—review and editing, G.D. and C.C.F.; Visualization, G.D. and M.P.; Supervision, F.R., M.N.R. and L.B.; Project administration, M.N.R. and L.B.; Funding acquisition, M.N.R. and L.B. All authors have read and agreed to the published version of the manuscript.

Funding: The research was funded by Project PRIN 2020, Sector ERC LS9 Call 2020 Prot. 2020 EMLWTN, CUP J83C20001990005 (G.D., E.C., M.N.R.) and partially funded under the National Recovery and Resilience Plan (NRRP), Mission 4 Component 2 Investment 1.4—Call for tender no. 3138 of 16 December 2021, rectified by Decree no. 3175 of 18 December 2021 of the Italian Ministry of University and Research funded by the European Union—NextGenerationEU. Award Number: Project code CN_00000033, Concession Decree No. 1034 of 17 June 2022 adopted by the Italian Ministry of University and Research, CUP, H43C22000530001, project title "National Biodiversity Future Center—NBFC" (M.P., L.B.). The research was carried out within the framework of the Ministry of University and Research (MUR) initiative "Departments of Excellence" (Law 232/2016), DIARC Project: "Habit—Inhabiting the Transition for rural constructions and agro-forestry territory" (C.C.F.) and DAFNE Project 2023-27 "Digital, Intelligent, Green and Sustainable (D.I.Ver.So)" (A.P.).

Data Availability Statement: PRISMA data can be obtained by registering at: https://prisma.asi.it/ (accessed on 20 December 2024). The ground truth collection used in this research as reference data for the classification step is available upon request by emailing the authors at: lorenzo.boccia@unina.it or at gabriele.delogu@unitus.it.

Acknowledgments: The authors would like to thank the Director of Serre Regional Park Authority, Francesco Maria Pititto, for providing the classification data of the Special Areas of Conservation and for participating and kindly assisting in the survey to collect the field data.

Conflicts of Interest: The authors declare that they have no known competing financial interests or personal relationships that could have appeared to influence the work reported in this paper.

References

1. Mittermeier, R.A.; Turner, W.R.; Larsen, F.W.; Brooks, T.M.; Gascon, C. Global Biodiversity Conservation: The Critical Role of Hotspots. In *Biodiversity Hotspots: Distribution and Protection of Conservation Priority Areas*; Zachos, F.E., Habel, J.C., Eds.; Springer: Berlin/Heidelberg, Germany, 2011; pp. 3–22, ISBN 978-3-642-20992-5.
2. Pallotta, E.; Boccia, L.; Rossi, C.M.; Ripa, M.N. Forest Dynamic in the Italian Apennines. *Appl. Sci.* **2022**, *12*, 2474. [CrossRef]
3. Randin, C.F.; Ashcroft, M.B.; Bolliger, J.; Cavender-Bares, J.; Coops, N.C.; Dullinger, S.; Dirnböck, T.; Eckert, S.; Ellis, E.; Fernández, N.; et al. Monitoring Biodiversity in the Anthropocene Using Remote Sensing in Species Distribution Models. *Remote Sens. Environ.* **2020**, *239*, 111626. [CrossRef]
4. Hansen, A.J.; Noble, B.P.; Veneros, J.; East, A.; Goetz, S.J.; Supples, C.; Watson, J.E.M.; Jantz, P.A.; Pillay, R.; Jetz, W.; et al. Toward Monitoring Forest Ecosystem Integrity within the Post-2020 Global Biodiversity Framework. *Conserv. Lett.* **2021**, *14*, e12822. [CrossRef]

5. Brockerhoff, E.G.; Barbaro, L.; Castagneyrol, B.; Forrester, D.I.; Gardiner, B.; González-Olabarria, J.R.; Lyver, P.O.; Meurisse, N.; Oxbrough, A.; Taki, H.; et al. Forest Biodiversity, Ecosystem Functioning and the Provision of Ecosystem Services. *Biodivers. Conserv.* **2017**, *26*, 3005–3035. [CrossRef]
6. Kacic, P.; Kuenzer, C. Forest Biodiversity Monitoring Based on Remotely Sensed Spectral Diversity—A Review. *Remote Sens.* **2022**, *14*, 5363. [CrossRef]
7. Malinowski, R.; Lewiński, S.; Rybicki, M.; Gromny, E.; Jenerowicz, M.; Krupiński, M.; Nowakowski, A.; Wojtkowski, C.; Krupiński, M.; Krätzschmar, E.; et al. Automated Production of a Land Cover/Use Map of Europe Based on Sentinel-2 Imagery. *Remote Sens.* **2020**, *12*, 3523. [CrossRef]
8. Casavecchia, S.; Allegrezza, M.; Biondi, E.; Galli, A.; Marcheggiani, E.; Pesaresi, S.; Taffetani, F.; Tavoletti, S.; Zitti, S.; Bianchelli, M.; et al. Conservation and Management of Biodiversity and Landscapes: A Challenge in the Era of Global Change. In *The First Outstanding 50 Years of "Università Politecnica delle Marche": Research Achievements in Life Sciences*; Longhi, S., Monteriù, A., Freddi, A., Aquilanti, L., Ceravolo, M.G., Carnevali, O., Giordano, M., Moroncini, G., Eds.; Springer International Publishing: Cham, Switzerland, 2020; pp. 483–503, ISBN 978-3-030-33832-9.
9. Goetz, S.J.; Baccini, A.; Laporte, N.T.; Johns, T.; Walker, W.; Kellndorfer, J.; Houghton, R.A.; Sun, M. Mapping and Monitoring Carbon Stocks with Satellite Observations: A Comparison of Methods. *Carbon Balance Manag.* **2009**, *4*, 2. [CrossRef] [PubMed]
10. Lim, J.; Kim, K.-M.; Jin, R. Tree Species Classification Using Hyperion and Sentinel-2 Data with Machine Learning in South Korea and China. *ISPRS Int. J. Geo-Inf.* **2019**, *8*, 150. [CrossRef]
11. Jia, J.; Wang, Y.; Chen, J.; Guo, R.; Shu, R.; Wang, J. Status and Application of Advanced Airborne Hyperspectral Imaging Technology: A Review. *Infrared Phys. Technol.* **2020**, *104*, 103115. [CrossRef]
12. Capolupo, A.; Kooistra, L.; Berendonk, C.; Boccia, L.; Suomalainen, J. Estimating Plant Traits of Grasslands from UAV-Acquired Hyperspectral Images: A Comparison of Statistical Approaches. *ISPRS Int. J. Geo-Inf.* **2015**, *4*, 2792–2820. [CrossRef]
13. Cogliati, S.; Sarti, F.; Chiarantini, L.; Cosi, M.; Lorusso, R.; Lopinto, E.; Miglietta, F.; Genesio, L.; Guanter, L.; Damm, A.; et al. The PRISMA Imaging Spectroscopy Mission: Overview and First Performance Analysis. *Remote Sens. Environ.* **2021**, *262*, 112499. [CrossRef]
14. Storch, T.; Honold, H.-P.; Chabrillat, S.; Habermeyer, M.; Tucker, P.; Brell, M.; Ohndorf, A.; Wirth, K.; Betz, M.; Kuchler, M.; et al. The EnMAP Imaging Spectroscopy Mission towards Operations. *Remote Sens. Environ.* **2023**, *294*, 113632. [CrossRef]
15. PRISMA Products Specification. Available online: https://prisma.asi.it/missionselect/docs/ (accessed on 30 July 2024).
16. Pepe, M.; Pompilio, L.; Gioli, B.; Busetto, L.; Boschetti, M. Detection and Classification of Non-Photosynthetic Vegetation from PRISMA Hyperspectral Data in Croplands. *Remote Sens.* **2020**, *12*, 3903. [CrossRef]
17. Tripathi, P.; Garg, R.D. Feature Extraction of Desis and Prisma Hyperspectral Remote Sensing Datasets for Geological Applications. *Int. Arch. Photogramm. Remote Sens. Spat. Inf. Sci.* **2021**, *44*, 169–173. [CrossRef]
18. Guanter, L.; Irakulis-Loitxate, I.; Gorroño, J.; Sánchez-García, E.; Cusworth, D.H.; Varon, D.J.; Cogliati, S.; Colombo, R. Mapping Methane Point Emissions with the PRISMA Spaceborne Imaging Spectrometer. *Remote Sens. Environ.* **2021**, *265*, 112671. [CrossRef]
19. Vangi, E.; D'amico, G.; Francini, S.; Giannetti, F.; Lasserre, B.; Marchetti, M.; Chirici, G. The New Hyperspectral Satellite Prisma: Imagery for Forest Types Discrimination. *Sensors* **2021**, *21*, 1182. [CrossRef]
20. Shaik, R.U.; Laneve, G.; Fusilli, L. An Automatic Procedure for Forest Fire Fuel Mapping Using Hyperspectral (PRISMA) Imagery: A Semi-Supervised Classification Approach. *Remote Sens.* **2022**, *14*, 1264. [CrossRef]
21. Spiller, D.; Ansalone, L.; Carotenuto, F.; Mathieu, P.P. Crop Type Mapping Using Prisma Hyperspectral Images and One-Dimensional Convolutional Neural Network. In Proceedings of the 2021 IEEE International Geoscience and Remote Sensing Symposium IGARSS, Brussels, Belgium, 11–16 July 2021; IEEE: Piscataway, NJ, USA, 2021; pp. 8166–8169.
22. Tagliabue, G.; Boschetti, M.; Bramati, G.; Candiani, G.; Colombo, R.; Nutini, F.; Pompilio, L.; Rivera-Caicedo, J.P.; Rossi, M.; Rossini, M.; et al. Hybrid Retrieval of Crop Traits from Multi-Temporal PRISMA Hyperspectral Imagery. *ISPRS J. Photogramm. Remote Sens.* **2022**, *187*, 362–377. [CrossRef]
23. Vavassori, A.; Oxoli, D.; Venuti, G.; Brovelli, M.A.; Mohamed, A.B.E.A.; Moazzam, A.; Siciliani de Cumis, M.; Sacco, P.; Tapete, D. PRISMA Hyperspectral Satellite Imagery Application to Local Climate Zones Mapping. *Int. Arch. Photogramm. Remote Sens. Spat. Inf. Sci.* **2024**, *XLVIII-1–2024*, 643–648. [CrossRef]
24. Hughes, G. On the Mean Accuracy of Statistical Pattern Recognizers. *IEEE Trans. Inf. Theory* **1968**, *14*, 55–63. [CrossRef]
25. Alonso, M.C.; Malpica, J.A.; de Agirre, A.M. Consequences of the Hughes Phenomenon on Some Classification Techniques. In Proceedings of the ASPRS 2001 Annual Conference, Milwaukee, WI, USA, 1–5 May 2011.
26. Richards, J.A.; Jia, X. *Remote Sensing Digital Image Analysis: An Introduction*, 4th ed.; Springer: Berlin/Heidelberg, Germany, 2006; ISBN 978-3-540-25128-6.
27. Hong, D.; Yokoya, N.; Chanussot, J.; Xu, J.; Zhu, X.X. Learning to Propagate Labels on Graphs: An Iterative Multitask Regression Framework for Semi-Supervised Hyperspectral Dimensionality Reduction. *ISPRS J. Photogramm. Remote Sens.* **2019**, *158*, 35–49. [CrossRef]
28. Landgrebe, D. Hyperspectral Image Data Analysis as a High Dimensional Signal Processing Problem. *IEEE Signal Process. Mag.* **2002**, *19*, 17–28. [CrossRef]
29. Martinez-Sanchez, L.; See, L.; Yordanov, M.; Verhegghen, A.; Elvekjaer, N.; Muraro, D.; d'Andrimont, R.; van der Velde, M. Automatic Classification of Land Cover from LUCAS In-Situ Landscape Photos Using Semantic Segmentation and a Random Forest Model. *Environ. Model. Softw.* **2024**, *172*, 105931. [CrossRef]

30. van der Velde, M.; Goeau, H.; Bonnet, P.; d'Andrimont, R.; Yordanov, M.; Affouard, A.; Claverie, M.; Czucz, B.; Elvekjaer, N.; Martinez-Sanchez, L.; et al. Pl@ntNet Crops: Merging Citizen Science Observations and Structured Survey Data to Improve Crop Recognition for Agri-Food-Environment Applications. *Environ. Res. Lett.* **2023**, *18*, 025005. [CrossRef]
31. Ferster, C.J.; Coops, N.C. Integrating Volunteered Smartphone Data with Multispectral Remote Sensing to Estimate Forest Fuels. *Int. J. Digit. Earth* **2016**, *9*, 171–196. [CrossRef]
32. Kosmala, M.; Crall, A.; Cheng, R.; Hufkens, K.; Henderson, S.; Richardson, A.D. Season Spotter: Using Citizen Science to Validate and Scale Plant Phenology from Near-Surface Remote Sensing. *Remote Sens.* **2016**, *8*, 726. [CrossRef]
33. Ghasemi, N.; Justo, J.A.; Celesti, M.; Despoisse, L.; Nieke, J. Onboard Processing of Hyperspectral Imagery: Deep Learning Advancements, Methodologies, Challenges, and Emerging Trends. *arXiv* **2024**, arXiv:2404.06526.
34. Ma, L.; Liu, Y.; Zhang, X.; Ye, Y.; Yin, G.; Johnson, B.A. Deep Learning in Remote Sensing Applications: A Meta-Analysis and Review. *ISPRS J. Photogramm. Remote Sens.* **2019**, *152*, 166–177. [CrossRef]
35. Lou, C.; Al-qaness, M.A.A.; AL-Alimi, D.; Dahou, A.; Abd Elaziz, M.; Abualigah, L.; Ewees, A.A. Land Use/Land Cover (LULC) Classification Using Hyperspectral Images: A Review. *Geo-Spat. Inf. Sci.* **2024**, *27*, 1–42. [CrossRef]
36. Signoroni, A.; Savardi, M.; Baronio, A.; Benini, S. Deep Learning Meets Hyperspectral Image Analysis: A Multidisciplinary Review. *J. Imaging* **2019**, *5*, 52. [CrossRef]
37. Sothe, C.; De Almeida, C.M.; Schimalski, M.B.; La Rosa, L.E.C.; Castro, J.D.B.; Feitosa, R.Q.; Dalponte, M.; Lima, C.L.; Liesenberg, V.; Miyoshi, G.T.; et al. Comparative Performance of Convolutional Neural Network Weighted and Conventional Support Vector Machine and Random Forest for Classifying Tree Species Using Hyperspectral and Photogrammetric Data. *GISci. Remote Sens.* **2020**, *57*, 369–394. [CrossRef]
38. Hasan, M.; Ullah, S.; Khan, M.J.; Khurshid, K. Comparative Analysis of SVM, Ann and Cnn for Classifying Vegetation Species Using Hyperspectral Thermal Infrared Data. *Int. Arch. Photogramm. Remote Sens. Spat. Inf. Sci.* **2019**, *42*, 1861–1868. [CrossRef]
39. Wang, Y.; Zhang, W.; Gao, R.; Jin, Z.; Wang, X. Recent Advances in the Application of Deep Learning Methods to Forestry. *Wood Sci. Technol.* **2021**, *55*, 1171–1202. [CrossRef]
40. Zhang, B.; Zhao, L.; Zhang, X. Three-Dimensional Convolutional Neural Network Model for Tree Species Classification Using Airborne Hyperspectral Images. *Remote Sens. Environ.* **2020**, *247*, 111938. [CrossRef]
41. Fassnacht, F.E.; Latifi, H.; Stereńczak, K.; Modzelewska, A.; Lefsky, M.; Waser, L.T.; Straub, C.; Ghosh, A. Review of Studies on Tree Species Classification from Remotely Sensed Data. *Remote Sens. Environ.* **2016**, *186*, 64–87. [CrossRef]
42. Zhong, L.; Dai, Z.; Fang, P.; Cao, Y.; Wang, L. A Review: Tree Species Classification Based on Remote Sensing Data and Classic Deep Learning-Based Methods. *Forests* **2024**, *15*, 852. [CrossRef]
43. Blickensdörfer, L.; Oehmichen, K.; Pflugmacher, D.; Kleinschmit, B.; Hostert, P. National Tree Species Mapping Using Sentinel-1/2 Time Series and German National Forest Inventory Data. *Remote Sens. Environ.* **2024**, *304*, 114069. [CrossRef]
44. Dalponte, M.; Bruzzone, L.; Gianelle, D. Tree Species Classification in the Southern Alps Based on the Fusion of Very High Geometrical Resolution Multispectral/Hyperspectral Images and LiDAR Data. *Remote Sens. Environ.* **2012**, *123*, 258–270. [CrossRef]
45. Shaik, R.; Periasamy, S.; Zeng, W. Potential Assessment of PRISMA Hyperspectral Imagery for Remote Sensing Applications. *Remote Sens.* **2023**, *15*, 1378. [CrossRef]
46. QField App. Available online: https://qfield.org/ (accessed on 4 November 2024).
47. EyeLand App. Available online: https://prineyeland.it/ (accessed on 4 November 2024).
48. Delogu, G.; Caputi, E.; Perretta, M.; Ripa, M.N.; Boccia, L. Using PRISMA Hyperspectral Data for Land Cover Classification with Artificial Intelligence Support. *Sustainability* **2023**, *15*, 13786. [CrossRef]
49. Hu, W.; Huang, Y.; Wei, L.; Zhang, F.; Li, H. Deep Convolutional Neural Networks for Hyperspectral Image Classification. *J. Sens.* **2015**, *2015*, 258619. [CrossRef]
50. Gasparini, P.; Di Cosmo, L.; Floris, A.; Notarangelo, G.; Rizzo, M. *Guida per i Rilievi in Campo. INFC2015—Terzo Inventario Forestale Nazionale*; Corpo Forestale dello Stato, Ministero per le Politiche Agricole, Alimentari e Forestali: Rome, Italy, 2016; ISBN 978-88-99595-44-9.
51. Parco Delle Serre. Available online: https://parcodelleserre.it/en/home-en/ (accessed on 3 May 2024).
52. Kottek, M.; Grieser, J.; Beck, C.; Rudolf, B.; Rubel, F. World Map of the Köppen-Geiger Climate Classification Updated. *Meteorol. Z.* **2006**, *15*, 259–263. [CrossRef] [PubMed]
53. Rubel, F.; Brugger, K.; Haslinger, K.; Auer, I. The Climate of the European Alps: Shift of Very High Resolution Köppen-Geiger Climate Zones 1800–2100. *Meteorol. Z.* **2017**, *26*, 115–125. [CrossRef]
54. Weather Data Archive. Available online: https://www.meteonetwork.eu/it/weather-station/clb110-stazione-meteorologica-di/archive (accessed on 4 November 2024).
55. Agnoletti, M. *Atlante dei Boschi Italiani*; I Robinson Letture, Prima edizione; Editori GLF Laterza: Bari, Italy, 2022; ISBN 978-88-581-4929-4.
56. Siviglia, M. *Biodiversità nel Parco Regionale delle Serre Calabresi. Territorio, Siti Naturali, Graniti, Cave, Piante Arboree, Flora, Funghi*; Rubbettino: Soveria Mannelli, Italy, 2023; ISBN 978-88-498-7397-9.
57. Hemmerling, J.; Pflugmacher, D.; Hostert, P. Mapping Temperate Forest Tree Species Using Dense Sentinel-2 Time Series. *Remote Sens. Environ.* **2021**, *267*, 112743. [CrossRef]

58. List of Sites of Community Importance. Available online: https://eur-lex.europa.eu/eli/dec_impl/2024/424/oj (accessed on 3 May 2024).
59. QGIS Geographic Information System; QGIS Association. Available online: https://www.qgis.org/ (accessed on 4 November 2024).
60. Caporusso, G.; Ettore, L.; Rino, L.; Rosa, L.; Rocchina, G.; Girolamo, D.M.; Patrizia, S. The Hyperspectral Prisma Mission in Operations. In Proceedings of the IGARSS 2020—2020 IEEE International Geoscience and Remote Sensing Symposium, Waikoloa, HI, USA, 26 September–2 October 2020; IEEE: Piscataway, NJ, USA, 2020; pp. 3282–3285.
61. LARP PrismaTool. Available online: https://github.com/LarpUnina/PrismaTool (accessed on 31 July 2024).
62. Alicandro, M.; Candigliota, E.; Dominici, D.; Immordino, F.; Masin, F.; Pascucci, N.; Quaresima, R.; Zollini, S. Hyperspectral PRISMA and Sentinel-2 Preliminary Assessment Comparison in Alba Fucens and Sinuessa Archaeological Sites (Italy). *Land* **2022**, *11*, 2070. [CrossRef]
63. Flynn, K.C.; Frazier, A.E.; Admas, S. Nutrient Prediction for Tef (Eragrostis Tef) Plant and Grain with Hyperspectral Data and Partial Least Squares Regression: Replicating Methods and Results across Environments. *Remote Sens.* **2020**, *12*, 2867. [CrossRef]
64. Cao, F.; Yang, Z.; Ren, J.; Mengying, J.; Ling, W.-K. Does Normalization Methods Play a Role for Hyperspectral Image Classification? *arXiv* **2017**, arXiv:1710.02939.
65. Huang, S.; Tang, L.; Hupy, J.P.; Wang, Y.; Shao, G. A Commentary Review on the Use of Normalized Difference Vegetation Index (NDVI) in the Era of Popular Remote Sensing. *J. For. Res.* **2021**, *32*, 1–6. [CrossRef]
66. Haboudane, D.; Miller, J.R.; Pattey, E.; Zarco-Tejada, P.J.; Strachan, I.B. Hyperspectral Vegetation Indices and Novel Algorithms for Predicting Green LAI of Crop Canopies: Modeling and Validation in the Context of Precision Agriculture. *Remote Sens. Environ.* **2004**, *90*, 337–352. [CrossRef]
67. Lemenkova, P.; Debeir, O. Computing Vegetation Indices from the Satellite Images Using GRASS GIS Scripts for Monitoring Mangrove Forests in the Coastal Landscapes of Niger Delta, Nigeria. *J. Mar. Sci. Eng.* **2023**, *11*, 871. [CrossRef]
68. Mehta, A.; Shukla, S.; Rakholia, S. Vegetation Change Analysis Using Normalized Difference Vegetation Index and Land Surface Temperature in Greater Gir Landscape. *J. Sci. Res.* **2021**, *65*, 01–06. [CrossRef]
69. Jolliffe, I.T. Principal Component Analysis and Factor Analysis. In *Principal Component Analysis*; Jolliffe, I.T., Ed.; Springer Series in Statistics; Springer: New York, NY, USA, 1986; pp. 115–128, ISBN 978-1-4757-1904-8.
70. Zhang, W.; Li, X.; Zhao, L. Band Priority Index: A Feature Selection Framework for Hyperspectral Imagery. *Remote Sens.* **2018**, *10*, 1095. [CrossRef]
71. Sawant, S.; Prabukumar, M. A Survey of Band Selection Techniques for Hyperspectral Image Classification. *J. Spectr. Imaging* **2020**, *9*, a5. [CrossRef]
72. Yang, H.; Chen, M.; Wu, G.; Wang, J.; Wang, Y.; Hong, Z. Double Deep Q-Network for Hyperspectral Image Band Selection in Land Cover Classification Applications. *Remote Sens.* **2023**, *15*, 682. [CrossRef]
73. Perretta, M.; Delogu, G.; Funsten, C.; Patriarca, A.; Caputi, E.; Boccia, L. Testing the Impact of Pansharpening Using PRISMA Hyperspectral Data: A Case Study Classifying Urban Trees in Naples, Italy. *Remote Sens.* **2024**, *16*, 3730. [CrossRef]
74. Lyngdoh, R.B.; Sahadevan, A.S.; Ahmad, T.; Rathore, P.S.; Mishra, M.; Gupta, P.K.; Misra, A. AVHYAS: A Free and Open Source QGIS Plugin for Advanced Hyperspectral Image Analysis. In Proceedings of the 2021 International Conference on Emerging Techniques in Computational Intelligence (ICETCI), Hyderabad, India, 25–27 August 2021.
75. Sen, O.; Keles, H.Y. On the Evaluation of CNN Models in Remote-Sensing Scene Classification Domain. *PFG J. Photogramm. Remote Sens. Geoinf. Sci.* **2020**, *88*, 477–492. [CrossRef]
76. Jena, B.; Saxena, S.; Nayak, G.K.; Saba, L.; Sharma, N.; Suri, J.S. Artificial Intelligence-Based Hybrid Deep Learning Models for Image Classification: The First Narrative Review. *Comput. Biol. Med.* **2021**, *137*, 104803. [CrossRef]
77. Congalton, R. Accuracy Assessment and Validation of Remotely Sensed and Other Spatial Information. *Int. J. Wildland Fire* **2001**, *10*, 321–328. [CrossRef]
78. Grandini, M.; Bagli, E.; Visani, G. Metrics for Multi-Class Classification: An Overview. *arXiv* **2020**, arXiv:2008.05756.
79. Naidu, G.; Zuva, T.; Sibanda, E.M. A Review of Evaluation Metrics in Machine Learning Algorithms. In *Artificial Intelligence Application in Networks and Systems, Proceedings of the 12th Computer Science On-Line Conference 2023, Online, 3–5 April 2023*; Silhavy, R., Silhavy, P., Eds.; Springer International Publishing: Cham, Switzerland, 2023; pp. 15–25.
80. Congedo, L. Semi-Automatic Classification Plugin: A Python Tool for the Download and Processing of Remote Sensing Images in QGIS. *J. Open Source Softw.* **2021**, *6*, 3172. [CrossRef]
81. Bandyopadhyay, D.; Mukherjee, S.; Ball, J.; Vincent, G.; Coomes, D.A.; Schönlieb, C.-B. Tree Species Classification from Hyperspectral Data Using Graph-Regularized Neural Networks. *arXiv* **2022**, arXiv:2208.08675.
82. Foody, G.M. Status of Land Cover Classification Accuracy Assessment. *Remote Sens. Environ.* **2002**, *80*, 185–201. [CrossRef]
83. Goodenough, D.G.; Dyk, A.; Niemann, K.O.; Pearlman, J.S.; Chen, H.; Han, T.; Murdoch, M.; West, C. Processing Hyperion and ALI for Forest Classification. *IEEE Trans. Geosci. Remote Sens.* **2003**, *41*, 1321–1331. [CrossRef]
84. Heikkinen, V.; Tokola, T.; Parkkinen, J.; Korpela, I.; Jaaskelainen, T. Simulated Multispectral Imagery for Tree Species Classification Using Support Vector Machines. *IEEE Trans. Geosci. Remote Sens.* **2010**, *48*, 1355–1364. [CrossRef]
85. Korpela, I.; Ørka, H.O.; Hyyppä, J.; Heikkinen, V.; Tokola, T. Range and AGC Normalization in Airborne Discrete-Return LiDAR Intensity Data for Forest Canopies. *ISPRS J. Photogramm. Remote Sens.* **2010**, *65*, 369–379. [CrossRef]

86. Thomlinson, J.R.; Bolstad, P.V.; Cohen, W.B. Coordinating Methodologies for Scaling Landcover Classifications from Site-Specific to Global: Steps toward Validating Global Map Products. *Remote Sens. Environ.* **1999**, *70*, 16–28. [CrossRef]
87. Rogers, J.A.; Robertson, K.M.; Hawbaker, T.J.; Sousa, D.J. Classifying Plant Communities in the North American Coastal Plain With PRISMA Spaceborne Hyperspectral Imagery and the Spectral Mixture Residual. *J. Geophys. Res. Biogeosci.* **2024**, *129*, e2024JG008217. [CrossRef]
88. Vanguri, R.; Laneve, G.; Hościło, A. Mapping Forest Tree Species and Its Biodiversity Using EnMAP Hyperspectral Data along with Sentinel-2 Temporal Data: An Approach of Tree Species Classification and Diversity Indices. *Ecol. Indic.* **2024**, *167*, 112671. [CrossRef]
89. Fricker, G.A.; Ventura, J.D.; Wolf, J.A.; North, M.P.; Davis, F.W.; Franklin, J. A Convolutional Neural Network Classifier Identifies Tree Species in Mixed-Conifer Forest from Hyperspectral Imagery. *Remote Sens.* **2019**, *11*, 2326. [CrossRef]
90. Liu, M.; Yu, T.; Gu, X.; Sun, Z.; Yang, J.; Zhang, Z.; Mi, X.; Cao, W.; Li, J. The Impact of Spatial Resolution on the Classification of Vegetation Types in Highly Fragmented Planting Areas Based on Unmanned Aerial Vehicle Hyperspectral Images. *Remote Sens.* **2020**, *12*, 146. [CrossRef]
91. Palsson, B.; Sigurdsson, J.; Sveinsson, J.R.; Ulfarsson, M.O. Hyperspectral Unmixing Using a Neural Network Autoencoder. *IEEE Access* **2018**, *6*, 25646–25656. [CrossRef]
92. Alparone, L.; Arienzo, A.; Garzelli, A. Spatial Resolution Enhancement of Satellite Hyperspectral Data Via Nested Hyper-Sharpening With Sentinel-2 Multispectral Data. *IEEE J. Sel. Top. Appl. Earth Obs. Remote Sens.* **2024**, *17*, 10956–10966. [CrossRef]